Computers and Electronics in Agriculture 219 (2024) 108806

Contents lists available at ScienceDirect

Computers and Electronics in Agriculture

journal homepage: www.elsevier.com/locate/compag

Original papers

Estimation of the height profile of the path for autonomous driving in terrain☆

Tabish Badar [a,*], Issouf Ouattara [a], Juha Backman [a,b], Arto Visala [a]

[a] Department of Electrical Engineering and Automation, Aalto University, Maarintie 8, Espoo, 02150, Finland
[b] Digital technologies in agriculture, Natural Resources Institute Finland (Luke), Lönnrotinkatu 7, Mikkeli, 50100, Finland

ARTICLE INFO

Keywords:
3D elevation model
Autonomous ground vehicles
Forest machines
Drone mapping
Simultaneous localization and mapping

ABSTRACT

A priori knowledge about the height profile of the path is vital for rollover avoidance in the context of autonomous driving through uneven forest ground. The forest ground is usually covered with either soft vegetation in summertime, or by snow in winter. Thus, the exact solid form of the forest ground cannot be detected by camera or LiDAR. This article, we propose height-odometry and aided height-odometry methods for ground height estimation. The height-odometry method depends solely on interoceptive and proprioceptive sensor data, while the aided height-odometry combines height-odometry output with the existing 3D map information. Thus, the central idea is to build a reference 3D path for autonomous forest machines where the spatial positioning – based on the RTK-GNSS or Forest SLAM method – is fused with the output of (aided) height-odometry method(s). We evaluate the proposed height-odometry methods in two separate environments that are accurately (3D) mapped by a UAV using the advanced machine-vision-based SfM method and the LiDAR-based SLAM algorithms. Through comprehensive data analysis, we demonstrate that the proposed 3D path estimation methods are practical and simple to implement, yet sufficient to estimate the height profile of the path with desired accuracy.

1. Introduction

A classic machine chain in forest harvesting combines a harvester and a forwarder. The harvester is used for felling, debranching, and cutting the stem to logs, whereas the forwarder carries the logs to the roadside. Then, the trucks transport the logs to sawmills and factories. Such a machine chain, particularly a fully loaded forwarder, may seriously damage the forest ground (Mohieddinne et al., 2019). Such damage may exacerbate over time due to short winters because of climate change. Thus, lighter forwarders are needed, for example, two autonomous forwarders serving one semi-autonomous harvester, where the – semi-autonomous human-operated – harvester determines the spatial paths for the autonomous forwarder during harvesting. For autonomous operations of forwarders, 3D path estimation becomes crucial especially, in motion control to avoid rollover caused by slopes, stones, and stumps of harvested trees.

In the forestry case, a human-driven harvester shows the 2D (spatial) paths for the machines that follow. An accurate spatial position of the machine in open areas can be based on a real-time kinematics-corrected global navigation satellite system (RTK-GNSS), which provides centimeter-level positioning precision. However, the positioning done by RTK-GNSS is not accurate in dense forests. Although, the differential GPS works in such scenarios, its accuracy is about 2–3 m, which is not sufficient for 2D path determination. Thus, accurate spatial positioning in the forest is obtained using a map of trees built using LiDAR-based simultaneous localization and mapping (Forest SLAM) algorithms (see, for example, Chen et al., 2020; Pierzchała et al., 2018; Tang et al., 2015; Miettinen et al., 2007; Hyyti and Visala, 2013 for relevant discussions).

The current literature on ground height estimation, however, is limited to methods that either estimate the roughness profile of the ground (see, for example, González et al. (2008) and the references within) or avoid sudden potholes (Xue et al., 2017). In other studies, such as Broggi et al. (2013), Jaspers et al. (2017), Forkel et al. (2021), the primary data used for the estimation of the 3D form of the terrain is a 3D point cloud derived either from LiDAR, a camera, or a combination of these two sensors mounted on the vehicles. However, in winter conditions where the ground is covered by snow, the methods relying on point clouds can only determine the 3D form of the surface of the snow, not the underlying solid ground. In summer, the point cloud represents the surface of ground vegetation. In other situations, such

☆ The research is funded by the Technology Industries of Finland Centennial Foundation and Jane and Aatos Erkko Foundation, Finland.
* Corresponding author.
E-mail address: tabish.badar@aalto.fi (T. Badar).

https://doi.org/10.1016/j.compag.2024.108806
Received 3 October 2023; Received in revised form 26 January 2024; Accepted 28 February 2024
Available online 10 March 2024

methods are limited as the ground's height profile has to be known before, for example, thinning-cutting harvesting.

Therefore, the LiDAR-based methods and camera-based methods are insufficient in measuring the solid form of the ground. In this study, the central idea is to use the vertical wheel displacement information with the vehicle's attitude information to obtain an accurate height profile of the path. This study is unique in the sense that we propose that the first machine (i.e., a harvester) goes through the forest, determines the spatial path based on the map of trees, and estimates the height profile of the path for the machines coming later. Eventually, the generated *3D reference path* is used by other machines in the autonomous driving context. An initial study was conducted in Badar et al. (2023) to measure the vertical displacement of each wheel over the ground. It depicts a *basic method* that relies on the altitude information provided by the exteroceptive sensor (RTK-GNSS) to estimate the *instantaneous* height of each wheel over the ground. Moreover, the experiments in Badar et al. (2023) were limited to open areas exclusively. Here, we extend our investigation on ground height estimation using a set of interoceptive sensors and sparse *a priori* 3D map information in both open and covered areas for the reasons discussed above.

The usage of unmanned aerial vehicles (UAVs) for building a 3D terrain model is an enhanced technology (Ouattara et al., 2022). Thus, we can generate dense 3D models of the terrain using a camera or a LiDAR mounted on a UAV. Such reference modeling methods can achieve centimeter-level accuracy when ground control points are used as described in Sanz-Ablanedo et al. (2018), Jiménez-Jiménez et al. (2021). In Badar et al. (2023), overlapping images from a UAV stamped with RTK-GNSS information were utilized to produce a reference 3D model of the environment using commercial software. The reference 3D model generated by this method was used as the ground truth to verify the results from *basic* 3D path estimation method. For the forest case, due to the lack of accurate GNSS reception under the forest canopy, SLAM with *loop closure* method proposed in Ouattara et al. (2022) can be used to build a reference 3D model of the environment. The resulting map using the SLAM method with loop closure can then be aligned with an existing open-source 3D point cloud data to obtain accurate position referencing.

The organization of the paper is as follows. A brief detail about the instrumentation of the ground vehicle under study, i.e. Polaris electric all-terrain-vehicle (e-ATV), is presented in Section 2. In Section 3, the proposed 3D path estimation methods are described. The experiment results obtained from Polaris e-ATV data using the proposed methods are presented in Section 4. In the same section, we briefly present the UAV-based methods to build reference 3D models of the open area (Vakola test tracks) and covered area (forest test track) to validate our results. The results from each ground height estimation method are then compared to these UAV-based reference elevation models in Section 5. Finally, the conclusive remarks are made in Section 6, where we also highlight the prospects of this study in our future work.

2. Polaris e-ATV instrumentation

Polaris Ranger, as shown in Fig. 1, is the vehicle used in this study. It is 143.5 cm wide, 274.3 cm long, and 185.4 cm high. The front suspensions are MacPherson struts, while the dual A-arm suspension system is installed at the rear axle. Each Carlisle tire has a rating of 25 × 9–12 with a rated tire pressure of 137.9 kPa. The important sensors and electronic control units (ECUs) used in this are highlighted in Fig. 2 (we refer to Badar (2019) and the reference within for sensors' functionality and respective datasheets). Two EPEC 5050 ECUs are used for power steering and automatic speed control along with handling data from wheel encoders. In addition, it has a synchronous position, attitude, and navigation (SPAN) unit. It collects satellite data using Pinwheel's GNSS antenna and combines RTK corrections through a 4G data connection with its positioning data to achieve centimeter-level accuracy. For the proposed 3D-path estimation methods, we measured

Fig. 1. Polaris e-ATV used in this study is shown.

the vertical displacement Δ_k of the spring at each corner of the vehicle. To achieve this, a Hall-effect rotary position sensor was installed in every shaft joining the vehicle's main body to the center of the kth wheel. Four sensor mount assemblies were printed using a 3D printer and installed on each shaft. Each rotary sensor outputs voltage in a linearly distributed angular measurement range.

In this study, we are using RTK-GNSS-based position data reported by the SPAN unit. $\mathbf{P}_{\text{GNSS}}$ contains the position information of the GNSS antenna in the global frame. The RTK corrections are needed to get the positioning data at an accuracy of 1 cm. Moreover, the accurate position of each wheel in the global coordinate system is needed, which depends on the attitude given by SPAN and several vehicle parameters. Primarily, we require wheelbase (l), track width (t), and wheel radius (h_T) values. Furthermore, it is essential to precisely know the longitudinal, lateral, and height distances namely; x_{off}, y_{off}, and h_{off}, from the GNSS antenna position on Polaris e-ATV to the center of the vehicle (CV). Moreover, pitch angle and roll angle offsets represented by θ_{off} and ϕ_{off} respectively, are expected due to probable SPAN installation issues on Polaris. Thus, the crucial parameters influencing the accuracy of the 3D form estimation are $x_{\text{off}}, y_{\text{off}}, h_{\text{off}}, l, t, h_T$, along with θ_{off} and ϕ_{off}. The procedure to obtain the optimal estimates of these parameters is discussed in great detail in Badar et al. (2023).

3. Estimation of height profiles

In this section, we focus on the proposed height estimation methods using Polaris e-ATV. First, we mention the *basic method* for 3D path estimation from Badar et al. (2023), which fuses the vertical wheel deflection and vehicle attitude data with the position and height information from RTK-GNSS to obtain the height profile of the ground. Its limitations will become evident when we compare its 3D path estimation accuracy with the proposed height-odometry methods in the forest environment.

3.1. Basic method

To get the 3D form of the ground, we need the position of each wheel in the global frame. The equation that describes the position of the wheel-ground contact patch in the global frame of reference is given as (Badar et al., 2023):

$$\mathbf{P}_k = \mathbf{C}_b^G(-\mathbf{P}_{b,\text{off}} + \mathbf{P}_{b,k}) + \mathbf{P}_{\text{GNSS}} + \begin{bmatrix} 0 \\ 0 \\ -\Delta_k - h_T \end{bmatrix}, \tag{1}$$

where the subscript (k) represents front left (FL), front right (FR), rear left (RL), and rear right (RR) tires or strut-mount points respectively.

(a) EPEC 5050 Control Unit

(b) SPAN-IGM-S1 Unit

(c) Pinwheel's GNSS Antenna

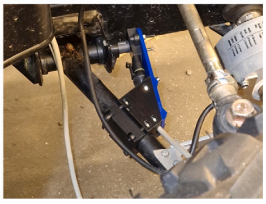

(d) Honeywell's Hall-effect Sensor

Fig. 2. Electronics systems available in Polaris.

In the above equation, $\mathbf{C}_b^G$ is the body frame to a global frame rotation matrix, defined as

$$\mathbf{C}_b^G = \mathbf{R}_z(\psi)\mathbf{R}_y(\theta - \theta_{\text{off}})\mathbf{R}_x(\phi - \phi_{\text{off}}),$$

where $\mathbf{R}_x(\cdot)$, $\mathbf{R}_y(\cdot)$, and $\mathbf{R}_z(\cdot)$ are the rotation matrices (see, for example, Etkin and Reid, 1995 for their definition). Moreover, the position vectors are defined as

$$\mathbf{P}_{b,\text{off}} = \begin{bmatrix} x_{\text{off}} \\ y_{\text{off}} \\ h_{\text{off}} \end{bmatrix}; \mathbf{P}_{b,k} = \begin{bmatrix} l_k/2 \\ t_k/2 \\ h_k/2 \end{bmatrix}; \mathbf{P}_{\text{GNSS}} = \begin{bmatrix} \text{X}_{\text{GNSS}} \\ \text{Y}_{\text{GNSS}} \\ \text{Z}_{\text{GNSS}} \end{bmatrix} \tag{2}$$

where $\mathbf{P}_{b,\text{off}}$ contains the offset values between the position of the GNSS antenna and the center of the vehicle (CV) in the body frame. $\mathbf{P}_{b,k}$ represents the distance of the kth tire from the CV in body frame. Thus, $l_k/2$ is longitudinal, $t_k/2$ is lateral, and $h_k/2 = h_{\text{off}}$ is the vertical distance between the kth center of each wheel and CV. Notice that the position vector $\mathbf{P}_{b,k}$ is defined in terms of wheelbase, track width, and box height after sign adjustments when the origin $(0, 0, 0)$ of the vehicle is assumed to be at the CV. In Eq. (1), Δ_k represents the measured instantaneous displacements of the kth spring. Hence, the basic method implies the estimation of the 3D form of the path using Eq. (1) provided the vehicle parameters, and pose measurements are known to centimeter-level accuracy.

3.2. Height-odometry method

In the dense forest, we cannot measure accurately the position of the vehicle, including the height with GNSS. Thus, we present the *height-odometry method* to compute the 3D form of the path traveled by each wheel. This method estimates the 3D form of the path using the front wheel height measurements, attitude measurements, vehicle geometry, and rear wheel height measurements since when driving forward, the rear wheels move in the already modeled 3D path. We encapsulate the proposed method in the form of an algorithm executed as a pseudo-code given below:

Algorithm I: **Height-Odometry Estimation**

Step 1: Read 2D position, i.e., $(\text{X}_{\text{SEN}}, \text{Y}_{\text{SEN}})$ coordinates of the (preferred positioning) sensor in the global frame of reference; roll (ϕ), pitch (θ), and yaw (ψ) angles from the IMU; and vertical displacement of each wheel (Δ_k) using

$$\begin{aligned} \Delta_k &= H_k - H_{k,0} \\ &= \mathcal{K}_{H,k} V_k + C_{H,k} + \frac{C_{m,k}}{\mathcal{K}_{m,k}}. \end{aligned} \tag{3}$$

Step 2: Using sensor values, calculate the $(\text{X}_{k,\text{ODO}}, \text{Y}_{k,\text{ODO}})$ coordinates of the rear wheels using Eq. (1), i.e., for $k \in \{\text{RR}, \text{RL}\}$.

Step 3: Locate the spatial positions of the rear wheels in the global frame of reference and read the height values in those locations from the created **map** using *height-odometry* such that

$$\text{Z}_{k,\text{ODO}} = \textbf{map}\left(\text{X}_k, \text{Y}_k\right) \tag{4}$$

where $k \in \{\text{RR}, \text{RL}\}$ at this step.

Step 4: Once $\mathbf{P}_{k,\text{ODO}} = (\text{X}_{k,\text{ODO}}, \text{Y}_{k,\text{ODO}}, \text{Z}_{k,\text{ODO}})$ positions of the rear wheels are known using the **map**, compute the location of the vehicle center (VC) by averaging the positions of the rear wheels such that

$$\begin{aligned} \mathbf{P}_{\text{VC,ODO}} = \frac{1}{2}\left(\mathbf{P}_{\text{RL,ODO}} - \mathbf{C}_b^G \mathbf{P}_{b,\text{RL}} - \begin{bmatrix} 0 \\ 0 \\ -\Delta_{\text{RL}} - h_T \end{bmatrix}\right) + \\ \frac{1}{2}\left(\mathbf{P}_{\text{RR,ODO}} - \mathbf{C}_b^G \mathbf{P}_{b,\text{RR}} - \begin{bmatrix} 0 \\ 0 \\ -\Delta_{\text{RR}} - h_T \end{bmatrix}\right). \end{aligned} \tag{5}$$

Step 5: Using the global position of vehicle center $\mathbf{P}_{\text{VC,ODO}}$, calculate the position of the front wheels from Eq. (1), such that

$$\mathbf{P}_{k,\text{ODO}} = \mathbf{P}_{\text{VC,ODO}} + \mathbf{C}_b^G \mathbf{P}_{b,k} + \begin{bmatrix} 0 \\ 0 \\ -\Delta_k - h_T \end{bmatrix} \tag{6}$$

where $k \in \{\text{FR}, \text{FL}\}$ at this stage.

Step 6: Update the **map** using the *location history* of the front wheels such that

$$\textbf{map} = \mathbf{J}\left(\begin{bmatrix} \bar{\text{X}}_{\text{FR,ODO}} \\ \bar{\text{X}}_{\text{FL,ODO}} \end{bmatrix}, \begin{bmatrix} \bar{\text{Y}}_{\text{FR,ODO}} \\ \bar{\text{Y}}_{\text{FL,ODO}} \end{bmatrix}, \begin{bmatrix} \bar{\text{Z}}_{\text{FR,ODO}} \\ \bar{\text{Z}}_{\text{FL,ODO}} \end{bmatrix}\right) \tag{7}$$

where, as an example, $\bar{\text{Z}}_{k,\text{ODO}} = \{\text{Z}^{\text{a}}_{k,\text{ODO}}, \ldots, \text{Z}^{\text{b}}_{k,\text{ODO}}\}$ is a column vector that contains the elevations underneath the front wheels between point **a** and **b** in the inertial frame. In the above equation, $\mathbf{J}(\cdot)$ is a *multivariate linear interpolation* function.

3.3. Aided height-odometry method

It is important to mention here that Algorithm I does not incorporate any corrections while computing $\text{Z}_{k,\text{ODO}}$. In general, a limitation of the odometry-based method is that the quantities (position, or height) suffer a loss of accuracy over time as errors accumulate. Thus, to overcome such limitations, we formulate the *aided height-odometry method*.

For this method, we assume that a 3D model of the region of interest (ROI) is available. It is the case, for example, in Finland that all the forests have been scanned with airborne LiDAR. This *a priori* 3D map is provided by the National Land Survey of Finland (NLS), which is a low-resolution (sparse), open-source, laser point-cloud data suitable for real-time applications.

Here, we state an *offline* or a *batch* version of this method, i.e., assuming that we have already built a **map** using Algorithm I, and the *a priori* 3D map information corrects the accumulated errors. Thus, we define

$$\mathbf{map}_{\mathrm{PRI}} = \mathbf{J}\left(\left[\tilde{\mathrm{X}}_{\mathrm{PRI}}, \tilde{\mathrm{Y}}_{\mathrm{PRI}}, \tilde{\mathrm{Z}}_{\mathrm{PRI}}\right]\right), \tag{8}$$

such that the interpolation function $\mathbf{J}(\cdot)$ incorporates all the 3D location points of the ROI provided in the reference 3D model. In Eq. (8), $\tilde{\mathrm{X}}_{\mathrm{PRI}}$, $\tilde{\mathrm{Y}}_{\mathrm{PRI}}$, and $\tilde{\mathrm{Z}}_{\mathrm{PRI}}$ are the column vectors. Thus, once $\mathbf{map}_{\mathrm{PRI}}$ is obtained from Eq. (8), we can read the height ($\mathrm{Z}_{k,\mathrm{PRI}}$) of each wheel using

$$\mathrm{Z}_{k,\mathrm{PRI}} = \mathbf{map}_{\mathrm{PRI}}\left(\mathrm{X}_{k,\mathrm{ODO}}, \mathrm{Y}_{k,\mathrm{ODO}}\right). \tag{9}$$

Then, the fundamental notion is to obtain the Aided height-ODometry (AOD) ($\mathrm{Z}_{k,\mathrm{AOD}}$) of kth wheel by fusing the two height measurements, $\mathrm{Z}_{k,\mathrm{ODO}}$ and $\mathrm{Z}_{k,\mathrm{PRI}}$ using a *spatial* complementary filter given as

$$\mathrm{Z}_{k,\mathrm{AOD}} = \mathrm{LPF}(\mathrm{Z}_{k,\mathrm{PRI}}, f_c) + \mathrm{HPF}(\mathrm{Z}_{k,\mathrm{ODO}}, f_c), \tag{10}$$

where $\mathrm{LPF}(\cdot)$ and $\mathrm{HPF}(\cdot)$ are the spatial versions of low-pass and high-pass filters respectively. Likewise, f_c is the spatial cutoff frequency in normalized units.

From Badar et al. (2023), we know that the wheel displacement sensors can accurately capture the instantaneous height variations of the path. However, due to limitations in the calibration procedure, the sensor outputs may be biased. Thus, the main reason for applying a high-pass filter on $\mathrm{Z}_{k,\mathrm{ODO}}$ is to remove the low (spatial) frequency components that cause $\mathrm{Z}_{k,\mathrm{ODO}}$ to (linearly) drift over time from the ground truth. Therefore, the aided height-odometry method incorporates corrections from *a priori* 3D map to get a filtered $\mathrm{Z}_{k,\mathrm{AOD}}$ for each wheel. Note that, the accuracy of the sparse *a priori* 3D map information directly affects the $\mathrm{Z}_{k,\mathrm{AOD}}$ data. However, we can address this limitation by proper tuning of the spatial cutoff frequency (f_c) in Eq. (10). Thus, we obtain $\mathrm{Z}_{k,\mathrm{AOD}}$ for each wheel that closely matches $\mathrm{Z}_{k,\mathrm{ODO}}$ in terms of ground variations while removing linear trends (or drifts) using the *a priori* 3D map.

In the next section, we present the important results from each ground height estimation method.

4. Results

For the open-area experiments, the concrete test tracks at Vakola, Vihti (Finland) facility were chosen. One particular set of data related to the counterclockwise driving of the Polaris e-ATV is collected to evaluate our methods. To test our methods in a forest environment, we also select a gravel track inside a nearby forest. At the time of the experiments, however, the forest was sparse as thinning-cutting harvesting was carried out recently. Therefore, in both test scenarios, we use the 2D position data from the SPAN unit as the spatial positions from RTK-GNSS were obtained with sufficient accuracy. However, before we present the main results, we first present the UAV-based reference 3D models that will be utilized to validate our ground height estimation methods later in Section 5.

4.1. Dense reference map by UAV system

Fig. 3 shows the images of the UAV systems used to produce the reference maps. To produce the dense reference 3D model of the Vakola test tracks, we employ a UAV equipped with a camera to capture images. These camera images are tagged with GNSS position from the onboard positioning unit. The GNSS positions are used as the initial pose of the camera by a structure from motion (SfM) and multi-view stereo matching (MVS) process which further refines the camera poses using the common features detected in different images (see Iglhaut et al., 2019 for a general presentation of the SfM-MVS photogrammetry process). First, a sparse point cloud is built during the camera pose estimation, and then a much-dense point cloud is built. From the dense point cloud, a depth map is built which can be used to generate a digital elevation model of the terrain. The MetaShape software is used in this study to produce the reference 3D model (Agisoft LLC, 2019). To improve the quality of the produced 3D model, 4 ground control points (GCPs) were used. According to Sanz-Ablanedo et al. (2018), using more than 3 GCPs for around 100 images will not improve the accuracy of the obtained 3D model.

Since the area surrounding the Vakola test facility is small, around 140 images were sufficient to build a 3D model of the Vakola test tracks. The GCPs positions were measured using an RTK-GNSS sensor with centimeter-level accuracy. The position of each ground control point is recorded for at least 30 s. The standard deviations of the altitude of the GCPs have values ranging from 2 mm to 4 mm which indicates a very stable altitude measurement. The produced 3D model from the drone data has RGB color information making it easier to pinpoint some locations on the model and verify their altitude measurement using manual methods. The accuracy of the RTK sensor used and the ability to manually check the altitude results make the 3D model produced from the UAV data a good choice as a reference 3D terrain model. Fig. 4, thus, illustrates the resulting 3D model.

To produce the dense reference map of the forest track, another UAV equipped with a LiDAR and IMU is used to collect data, which is processed using a SLAM framework with loop closure. An improved version of the SLAM framework proposed by Ouattara et al. (2022) is used. The SLAM framework leverages pose-graph optimization using the GTSAM framework (Dellaert et al., 2021) and loop closing to reduce the drift introduced by LiDAR odometry. The produced point cloud map by the SLAM framework is in the local coordinates of the starting point of the UAV flight. It was aligned with the NLS data (see, Section 4.2 for details about NLS data) to have both data in UTM coordinates using the open-source CloudCompare software (Anon, 2023). Fig. 5 shows the resulting 3D map after aligning the ground map from the SLAM method to the larger ground map from NLS data.

4.2. A priori (sparse, open-source) reference map

To obtain $\mathbf{map}_{\mathrm{PRI}}$ for the aided height-odometry method, elevation maps generated by methods such as those presented in Ouattara et al. (2022) and Kukko et al. (2017) can be utilized. The open-source 3D laser scanning data provided by the NLS of Finland is used to generate $\mathbf{map}_{\mathrm{PRI}}$ as it is sparse and requires less computational resources. This data has been used as additional ground truth data to verify results in Section 4.1. The point clouds of the ROIs, that is, the area around the test track and of the designated forest track are part of the point cloud data of map sheet number L4124G3 of the NLS database. It has a resolution of 1.77 points per squared meter with an elevation precision of 0.15 m. The point cloud data was captured by an airborne Lidar system flying at a 2044 m altitude in the year 2015. The 3D point cloud data of the Vakola tracks is shown in Fig. 6(a), which contains around 3,000 location points in a 70×70 m^2 grid. The 3D point cloud data concerning the forest track case is shown in Fig. 6(b). It is contained in the same map sheet as the Vakola test track. Notice that, only the ROI with data points classified as ground labels are extracted to be further used as $\mathbf{map}_{\mathrm{PRI}}$. Thus, we have $\mathbf{map}_{\mathrm{PRI}}$ for the forest drive test covering an area of 500×500 m^2 with 10,000 data points.

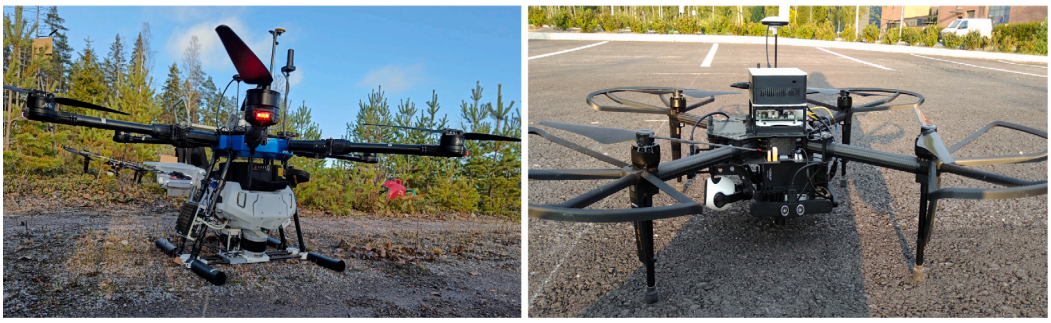

Fig. 3. The UAV system used to produce the reference map for the Vakola test track (left) and the dense reference map for the forest track (right).

Fig. 4. 3D model of the test tracks formed in Metashape using GNSS tagged camera images captured by drone and RTK-GNSS ground control points is shown.

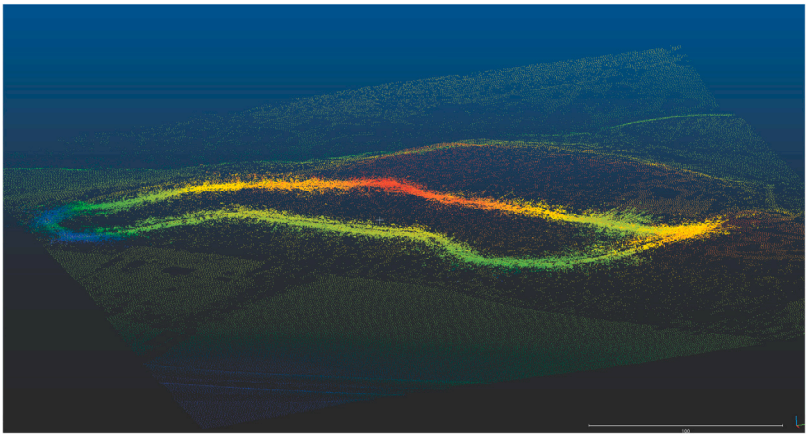

Fig. 5. The dense ground point cloud data from the SLAM method aligned with the larger NLS data.

4.3. 3D path estimation results

The driving trajectories of the wheels are obtained by employing the basic method. Notice that two loops on the Vakola test track were completed followed by driving toward the center of the track at the end. The cross represents the starting point, whereas the circle indicates the end-point of, for example, the GNSS trajectory in Fig. 7(a). In Fig. 7(b), we present the results from the basic method when the vehicle is driven on the forest track. In both test environments, $\mathbf{P}_{\text{GNSS}}$ is provided by the SPAN unit, whereas $\mathbf{P}_{\text{FR}}$ and $\mathbf{P}_{\text{RL}}$ are computed by using Eq. (1). Here, we show the position data for FR and RL wheels for brevity. Fig. 7, overall, depicts the spatial data in the Universal Traverse Mercator (UTM) coordinate system, whereas the height data is shown above the mean sea level.

Fig. 8 shows the main results of this study, which presents the solid form of the ground for FR and RL wheels using Algorithm I. Since we assume that no height is available beforehand, the initial heights of each trajectory start around 0 m. Note the accumulated errors in the height profiles in both test scenarios due to height odometry, which depicts the obvious limitation of this method. As mentioned above, we use the spatial location reported by the SPAN unit, i.e., $(X_{\text{SEN}}, Y_{\text{SEN}}) = (X_{\text{GNSS}}, Y_{\text{GNSS}})$. Since the spatial positions are RTK-corrected, we obtain spatial trajectories for each wheel with sufficient accuracy in both test scenarios.

To obtain the results from the aided height-odometry method, we first sample the height profile of the odometry method so that the distance traveled between two consecutive locations remains 3 cm, i.e., we define $ds = 0.03$ m. This is crucial as we have to apply the *spatial*

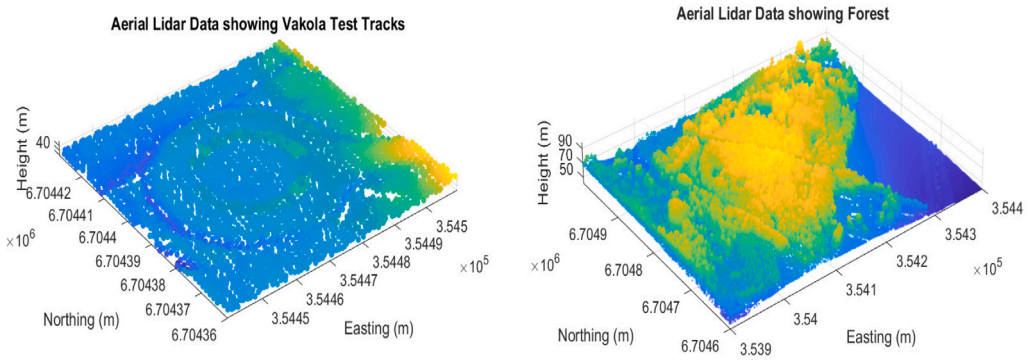

(a) Vakola Tracks (b) Forest Map

Fig. 6. The point cloud data provided by NLS for the test areas are shown.

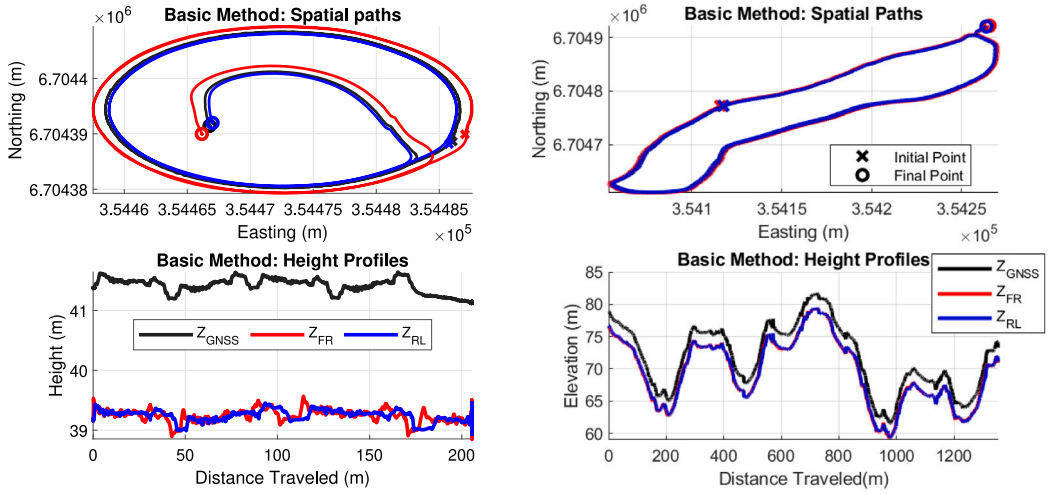

(a) Vakola Tracks (b) Forest Track

Fig. 7. The spatial paths of GNSS antenna (black), FR wheel (red), and RL wheel (blue) are shown for both test cases. Z_{GNSS} is from SPAN, whereas Z_{FR} and Z_{RL} are obtained from *basic method*.

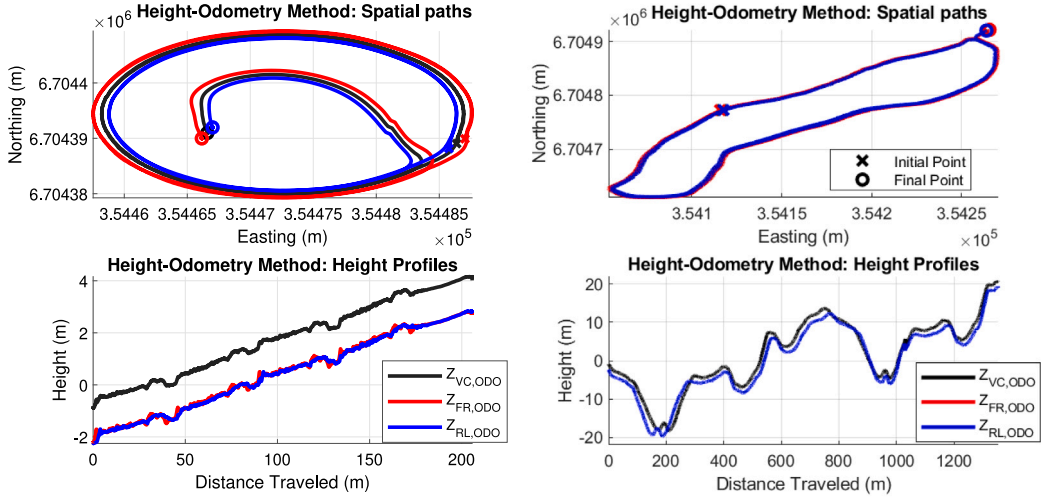

(a) Vakola Tracks (b) Forest Track

Fig. 8. 3D path estimation results are shown when the height-odometry method is employed.

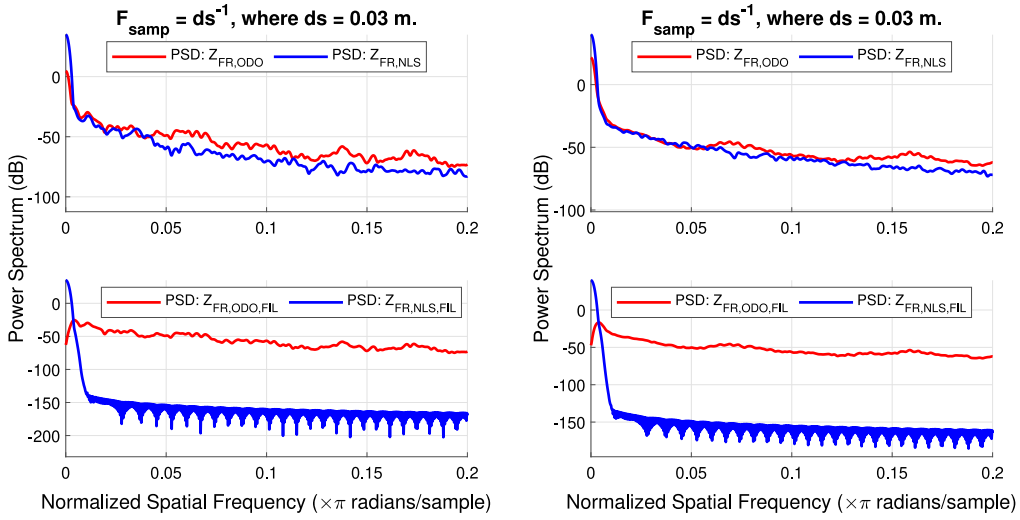

(a) Vakola Tracks (b) Forest Track

Fig. 9. The PSDs of the initial (top) and filtered (bottom) height data are shown.

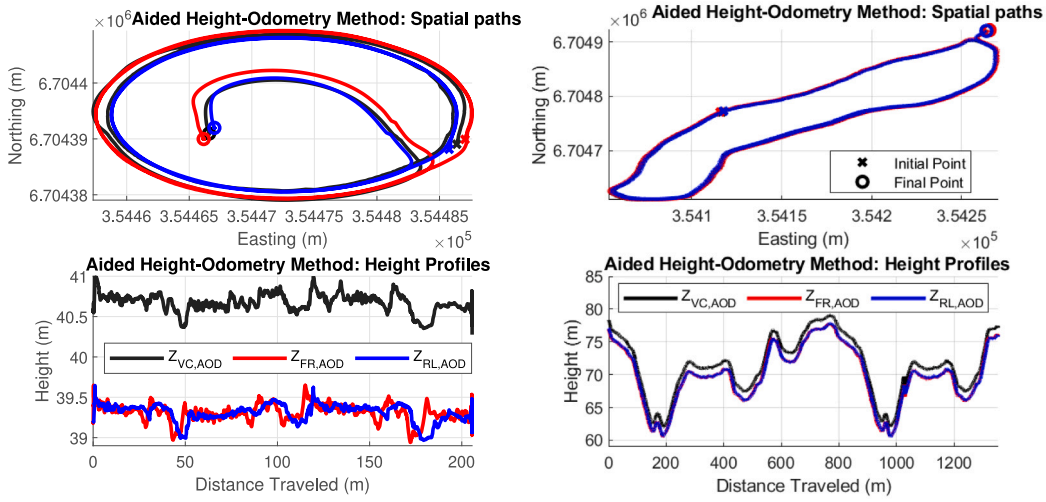

(a) Vakola Tracks (b) Forest Track

Fig. 10. Results from the aided height-odometry method are shown for both test cases.

versions of the low-pass and high-pass filters illustrated in Section 3.3. In other words, for f_c tuning, we need the power spectrum densities (PSDs) of the height profiles $Z_{k,\mathrm{ODO}}$, which we resample at $F_{\mathrm{samp}} = \mathrm{ds}^{-1}$.

Further, we interpolate the reference height data $Z_{k,\mathrm{NLS}}$ for each wheel using Eq. (9). We obtained these heights by using

$$Z_{k,\mathrm{NLS}} = \mathbf{map}_{\mathrm{PRI}}\left(X_{k,\mathrm{AOD}}, Y_{k,\mathrm{AOD}}\right)$$

where the inputs to $\mathbf{map}_{\mathrm{PRI}}$ are the re-sampled spatial paths from height-odometry and aided height-odometry methods such that at each instant the distance traveled is 0.03 m. In MATLAB, We utilized `scatteredInterpolant` function for the realization of $\mathbf{J}(\cdot)$ in Eq. (8) to create $\mathbf{map}_{\mathrm{PRI}}$ using point cloud data of the ROI. Fig. 9 illustrates the PSD analysis of the original ($Z_{k,\mathrm{ODO}}$ and $Z_{k,\mathrm{NLS}}$) heights and *filtered* ($Z_{k,\mathrm{ODO,FIL}}$ and $Z_{k,\mathrm{NLS,FIL}}$) heights. We obtained these PSDs for both test cases using the cutoff spatial frequency f_c of 0.003 $\times\pi$ radians per sample. Fig. 10 depicts the 3D paths obtained from the aided height-odometry method for the vehicle's center (VC) along with FR and RL wheels.

5. Discussion

Fig. 11(a) illustrates a zoomed-in perspective of the height estimated by the basic method in comparison to the reference map data generated by MetaShape. Fig. 11(b), likewise, compares the output of the basic method with the output of dense point cloud data using the SLAM method. The main disadvantage of the basic method, however, is highlighted in Fig. 11(b) when we compare the Z_k graphs with ground truth in the forest track case. Two particular instants, i.e., between 200–400 m and between 1000–1200 m (of distance traveled) are worth noting. The Z_k graphs deviate from $Z_{k,\mathrm{UAV}}$ upwards during the initial positions, whereas for the second positions, i.e., at *loop closure*, Z_k graphs report lower values. In addition, each Z_k graph has several jumps. Such anomalies in Z_k graphs produced by the basic method were obviously due to SPAN losing its accuracy in the forest. The loss rate of GNSS during the forest track case can be observed in Fig. 12, which depicts the standard deviations of latitude (σ_{LAT}), longitude (σ_{LAT}), and height (σ_{Z_G}) data reported by the SPAN unit. Thus, pointing out the

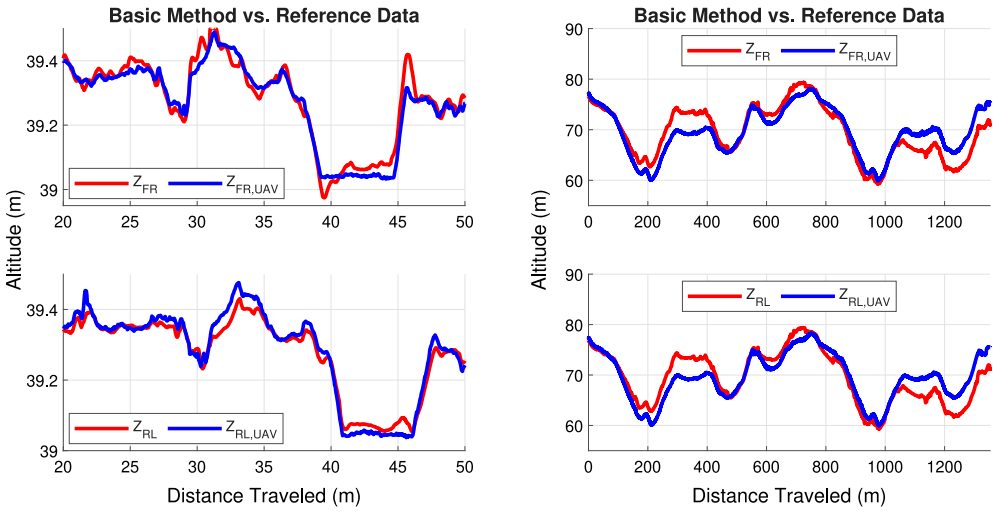

(a) Vakola Tracks (b) Forest Track

Fig. 11. Height estimated by the basic 3D-path estimation method (red) is compared to reference height data (blue) from the UAV-based SfM (left) and SLAM (right) methods.

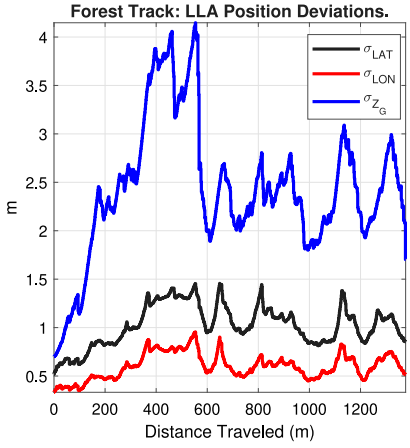

Fig. 12. Forest Track: Standard deviations of the latitude, longitude, and height data from SPAN are shown.

limitation of any path estimation method relying on height data from RTK-GNSS inside forests.

A comparison of the 3D path estimation results from height-odometry and aided height-odometry methods with the ground truth is illustrated in Fig. 13. For each wheel, $Z_{k,\mathrm{ODO}}$ (black) is the output of Algorithm I after removing the linear trend using `detrend` command in MATLAB. Further, we correct the initial height of $Z_{k,\mathrm{ODO}}$ using NLS data to obtain each graph in *absolute* height units. $Z_{k,\mathrm{AOD}}$ (red) are the heights that are obtained by combining height data from two methods using a complimentary filter. Note that, even after the manual removal of the drift from $Z_{k,\mathrm{ODO}}$ data there remains a constant bias from the ground truth. To examine the cause of bias in $Z_{k,\mathrm{ODO}}$ data, the equations for the height of front wheels used in Algorithm I are simplified as

$$Z_{\mathrm{FR}}^{\mathrm{current}} = \frac{1}{2}\left(Z_{\mathrm{RR}}^{\mathrm{map}} + Z_{\mathrm{RL}}^{\mathrm{map}}\right) - \frac{1}{2}\left(\Delta_{\mathrm{RR}}^{\mathrm{current}} + \Delta_{\mathrm{RL}}^{\mathrm{current}}\right) + \Delta_{\mathrm{FR}}^{\mathrm{current}}$$
$$Z_{\mathrm{FL}}^{\mathrm{current}} = \frac{1}{2}\left(Z_{\mathrm{RR}}^{\mathrm{map}} + Z_{\mathrm{RL}}^{\mathrm{map}}\right) - \frac{1}{2}\left(\Delta_{\mathrm{RR}}^{\mathrm{current}} + \Delta_{\mathrm{RL}}^{\mathrm{current}}\right) + \Delta_{\mathrm{FL}}^{\mathrm{current}}$$

which depicts the source of errors in odometric and aided-odometric methods to be Δ_k values. Consequently, we investigate the measured Δ_k values from the Vakola tracks case which are shown in Fig. 14. Furthermore, we present the root-mean-squared error (RMSE) values in Table 1 corresponding to the results from these two methods when

Table 1
Vakola Tracks: RMSEs comparing estimated and true heights for each wheel.

k	$\mathbf{E}_{k,\{\mathrm{ODO,UAV}\}}$	$\mathbf{E}_{k,\{\mathrm{AOD,UAV}\}}$	$\mathbf{E}_{k,\{\mathrm{NLS,UAV}\}}$	Units
FR	8.5888	4.1765	3.9906	cm
RR	9.4908	6.2046	3.6306	cm
FL	9.2557	3.5673	2.2736	cm
RL	9.1041	4.2569	2.3375	cm

UAV data is taken as ground truth. The $\mathbf{E}_{k,\{\mathrm{ODO,UAV}\}}$, e.g., represents the RMSE between $Z_{k,\mathrm{ODO}}$ (results from the odometric method after manual removal of trend in data) and $Z_{k,\mathrm{UAV}}$ (the ground truth obtained from MetaShape software) for the kth wheel. Notice that, Δ_{FL} in Fig. 14 displays higher values in comparison to other wheels since the driver sits in its vicinity, which correlates with the increased RMSE of 9.2557 cm in Table 1. This points out the only limitation of the spring deflection calibration procedure in Badar et al. (2023) that was performed in the absence of a driver. Nevertheless, identifying the solid form of the ground is notably more crucial for a vehicle's autonomous driving than knowing the terrain's true height, which Algorithms I predicts with sufficient accuracy in both test scenarios.

One can argue over the utilization of the more accurate, readily available, reference maps presented in Section 4.1 or Section 4.2 during real-time forest machine-chain operations instead of the height-odometry or aided height-odometry method. Let us consider that we use NLS data in a real-time scenario based on smallest error $\mathbf{E}_{k,\{\mathrm{NLS,UAV}\}}$ value in Table 1, which highlights that the NLS height data remain within 2–3 cm of the reference height data. Another advantage of using NLS data over UAV-based methods is its lower memory requirements as it is sparse. However, such a sparsity of the 3D map may lead to unexpected jumps in the *interpolated* altitudes as emphasized in Fig. 13(a) by the rectangular box. Secondly, and most importantly, such data is collected in the summertime, whereas in winter the forest's soft ground changes due to the compaction of snow caused by forest machines. Thus, the 3D point cloud of the ROI produced by NLS is not sufficient in the context of rollover avoidance.

6. Conclusions and future work

The accurate estimation of the 3D form of the solid ground is crucial for the stable operations of off-road vehicles. In this paper, we discussed three methods to estimate the height profile of the path. The results of the basic method in a GNSS-enabled environment (Vakola tracks case)

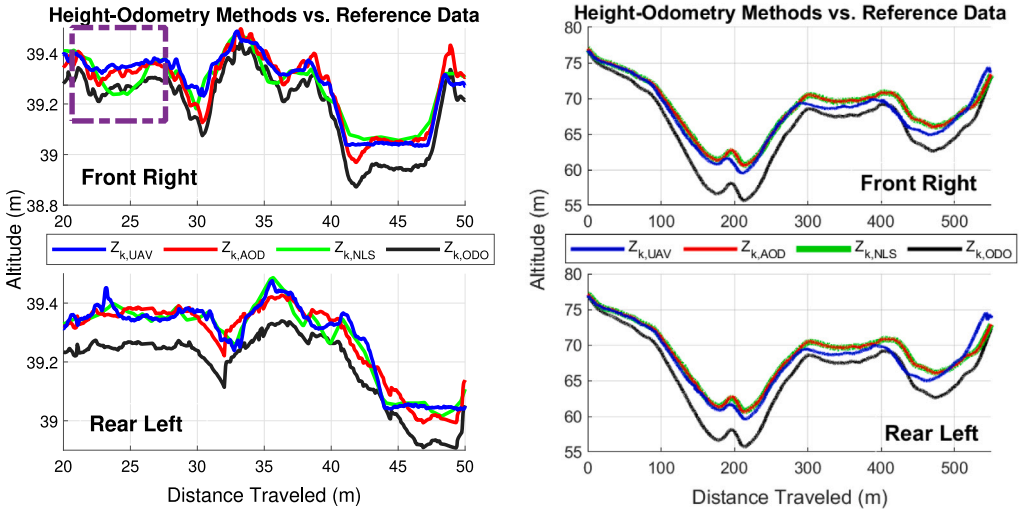

(a) Vakola Tracks (b) Forest Track

Fig. 13. The height estimated by the odometric (black) and aided-odometric methods (red) are compared to reference data from UAV (blue) and NLS (green).

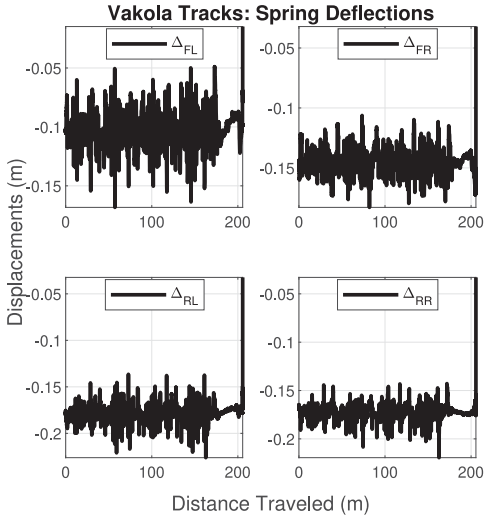

Fig. 14. Vakola Tracks: Spring deflection measurements are shown.

are promising and show the effectiveness of the instrumentation in the computation of the height profile of the path. However, its performance was deficient in the forest track case where the GNSS height measurements were erroneous. We introduced the height-odometry method which estimates the solid form of the ground using vehicle geometry, its orientation, and spring deflection information. The limitation of this method, however, concerns the bias and linear drift of wheel displacement sensors, and accumulated errors in general. The proposed aided height-odometry method corrects such errors in real-time by employing a *a priori* 3D map data, which applies a high-pass spatial filter on the output of the height odometry method and corrects it by incorporating the slow-varying absolute height information from the *a priori* map. The aided height-odometry method effectively overcomes the limitation of using a sparse *a priori* 3D map. The analysis of the results demonstrated an obvious advantage of (aided) height-odometry method(s) in identifying the solid form of the path when satellite-based navigation is not utilized. Therefore, this study answers the main research question, i.e., the variations in the ground profile – that are paramount to vehicle rollover avoidance – can be estimated with sufficient accuracy by Algorithm I.

In the future, when the machine size is smaller and the forwarder is autonomous, the forwarder may operate at the same time as the harvester. In such a scenario, the operator of the harvester supervises the forwarder as well. In this context, the harvester goes through the forest, creates a 2D path based on Forest SLAM, and estimates the height profile of the path using (aided) height-odometry method(s). In turn, it builds a *3D reference path* that is used by the autonomous forwarder that follows. The *validated* 3D reference path generated by the harvester can be sent to the autonomous forwarder over 4G/5G communication links. The autonomous forwarder employs a nonlinear model predictive control (NMPC) method for tracking the 3D reference path. The NMPC method avoids rollover by adjusting the speed of the vehicle based on the *future* 3D reference path.

CRediT authorship contribution statement

Tabish Badar: Data curation, Formal analysis, Investigation, Methodology, Software, Validation, Writing – original draft. **Issouf Ouattara:** Data curation, Methodology, Software, Investigation. **Juha Backman:** Conceptualization, Methodology, Supervision, Writing – review & editing. **Arto Visala:** Funding acquisition, Project administration, Supervision, Conceptualization, Resources, Writing – review & editing.

Declaration of competing interest

The authors declare that they have no known competing financial interests or personal relationships that could have appeared to influence the work reported in this paper.

Data availability

Data will be made available on request.

Acknowledgment

All authors approved the version of the manuscript to be published.

References

Agisoft LLC, 2019. Agisoft metashape user manual, professional edition, version 1.5.

Anon, 2023. CloudCompare, 3D point cloud and mesh processing software.

Badar, T., 2019. Implementation of the Autonomous Functionalities on an Electric Vehicle Platform for Research and Education (Master's thesis). School of Electrical Engineering, Aalto University.

Badar, T., Ouattara, I., Backman, J., Visala, A., 2023. Estimation of 3D form of the path for autonomous driving in terrain. IFAC-PapersOnLine 56 (02), 4916–4921.

Broggi, A., Cardarelli, E., Cattani, S., Sabbatelli, M., 2013. Terrain mapping for off-road Autonomous Ground Vehicles using rational B-spline surfaces and stereo vision. In: IEEE Intelligent Vehicles Symposium. IV, pp. 648–653.

Chen, S.W., Nardari, G.V., Lee, E.S., Qu, C., Liu, X., Romero, R.A.F., Kumar, V., 2020. SLOAM: Semantic lidar odometry and mapping for forest inventory. IEEE Robotics Autom. Lett. 5 (2), 612–619.

Dellaert, F., Roberts, R., Cunningham, A., Agrawal, V., Beall, C., Ta, D.-N., lucacarlone, Jiang, F., nikai, Blanco-Claraco, J.L., Williams, S., ydjian, Melim, A., Lv, Z., Dong, J., Lambert, J., Chande, K., Krishnan, A., Chen, G., balderdash-devil, DiffDecisionTrees, An, S., mpaluri, Mendes, E.P., Bosse, M., Patel, A., Baid, A., Furgale, P., matthewbroadwaynavenio, roderick-koehle, 2021. borglab/gtsam: 4.1.1. Zenodo.

Etkin, B., Reid, L.D., 1995. Dynamics of Flight: Stability and Control, third ed. John Wiley and Sons, USA.

Forkel, B., Kallwies, J., Wuensche, H.-J., 2021. Probabilistic terrain estimation for autonomous off-road driving. In: IEEE International Conference on Robotics and Automation. ICRA, pp. 13864–13870.

González, A., O'brien, E., Li, Y.-Y., Cashell, K., 2008. The use of vehicle acceleration measurements to estimate road roughness. Veh. Syst. Dyn. 46 (6), 483–499.

Hyyti, H., Visala, A., 2013. Feature based modeling and mapping of tree trunks and natural terrain using 3D laser scanner measurement system. IFAC Proc. Vol. 46 (10), 248–255, 8th IFAC Symposium on Intelligent Autonomous Vehicles.

Iglhaut, J., Cabo, C., Puliti, S., Piermattei, L., O'Connor, J., Rosette, J., 2019. Structure from motion photogrammetry in forestry: a review. Curr. For. Rep. 5.

Jaspers, H., Himmelsbach, M., Wuensche, H.-J., 2017. Multi-modal local terrain maps from vision and LiDAR. In: IEEE Intelligent Vehicles Symposium. IV, pp. 1119–1125.

Jiménez-Jiménez, S.I., Ojeda-Bustamante, W., Marcial-Pablo, M.d., Enciso, J., 2021. Digital terrain models generated with low-cost UAV photogrammetry: Methodology and accuracy. ISPRS Int. J. Geo-Inf. 10 (5).

Kukko, A., Kaijaluoto, R., Kaartinen, H., Lehtola, V.V., Jaakkola, A., Hyyppä, J., 2017. Graph SLAM correction for single scanner MLS forest data under boreal forest canopy. ISPRS J. Photogramm. Remote Sens. 132, 199–209.

Miettinen, M., Ohman, M., Visala, A., Forsman, P., 2007. Simultaneous localization and mapping for forest harvesters. In: Proceedings 2007 IEEE International Conference on Robotics and Automation. pp. 517–522.

Mohieddinne, H., Brasseur, B., Spicher, F., Gallet-Moron, E., Buridant, J., Kobaissi, A., Horen, H., 2019. Physical recovery of forest soil after compaction by heavy machines, revealed by penetration resistance over multiple decades. In: Forest Ecology and Management, vol. 449.

Ouattara, I., Korhonen, V., Visala, A., 2022. LiDAR-odometry based UAV pose estimation in young forest environment. IFAC-PapersOnLine 55 (32), 95–100.

Pierzchała, M., Giguère, P., Astrup, R., 2018. Mapping forests using an unmanned ground vehicle with 3D LiDAR and graph-SLAM. In: Computers and Electronics in Agriculture, vol. 145, pp. 217–225.

Sanz-Ablanedo, E., Chandler, J.H., Rodríguez-Pérez, J.R., Ordóñez, C., 2018. Accuracy of unmanned aerial vehicle (UAV) and SfM photogrammetry survey as a function of the number and location of ground control points used. Remote Sensing 10 (10).

Tang, J., Chen, Y., Kukko, A., Kaartinen, H., Jaakkola, A., Khoramshahi, E., Hakala, T., Hyyppä, J., Holopainen, M., Hyyppä, H., 2015. SLAM-aided stem mapping for forest inventory with small-footprint mobile LiDAR. Forests 6 (12), 4588–4606.

Xue, G., Zhu, H., Hu, Z., Yu, J., Zhu, Y., Luo, Y., 2017. Pothole in the dark: Perceiving pothole profiles with participatory urban vehicles. IEEE Trans. Mob. Comput. 16 (5), 1408–1419.